JOURNAL OF GEOPHYSICAL RESEARCH, VOL. 115, A04108, doi:10.1029/2009JA015094, 2010

Click Here for Full Article

Hybrid model of inhomogeneous solar wind plasma heating by Alfvén wave spectrum: Parametric studies

L. Ofman[1,2,3]

Received 11 November 2009; accepted 4 December 2009; published 30 April 2010.

[1] Observations of the solar wind plasma at 0.3 AU and beyond show that a turbulent spectrum of magnetic fluctuations is present. Remote sensing observations of the corona indicate that heavy ions are hotter than protons and their temperature is anisotropic ($T_\perp/T_\parallel \gg 1$). We study the heating and the acceleration of multi-ion plasma in the solar wind by a turbulent spectrum of Alfvénic fluctuations using a 2-D hybrid numerical model. In the hybrid model the protons and heavy ions are treated kinetically as particles, while the electrons are included as neutralizing background fluid. This is the first two-dimensional hybrid parametric study of the solar wind plasma that includes an input turbulent wave spectrum guided by observation with inhomogeneous background density. We also investigate the effects of He^{++} ion beams in the inhomogeneous background plasma density on the heating of the solar wind plasma. The 2-D hybrid model treats parallel and oblique waves, together with cross-field inhomogeneity, self-consistently. We investigate the parametric dependence of the perpendicular heating, and the temperature anisotropy in the H^+-He^{++} solar wind plasma. It was found that the scaling of the magnetic fluctuations power spectrum steepens in the higher-density regions, and the heating is channeled to these regions from the surrounding lower-density plasma due to wave refraction. The model parameters are applicable to the expected solar wind conditions at about 10 solar radii.

Citation: Ofman, L. (2010), Hybrid model of inhomogeneous solar wind plasma heating by Alfvén wave spectrum: Parametric studies, *J. Geophys. Res.*, *115*, A04108, doi:10.1029/2009JA015094.

1. Introduction

[2] In situ observations of the solar wind plasma at 0.3 AU and beyond by Helios, Ulysses, ACE, Wind, and STEREO spacecraft, as well as remote sensing observation by SOHO provide observational evidence for turbulent spectrum of magnetic fluctuations in the solar wind plasma. In particular, observations by Helios, Ulysses, and ACE, show that magnetic fluctuations in the solar wind can be fitted by simple power laws: f^{-1} in the millihertz range, $f^{-5/3}$ in the intermediate inertial range, and steeper spectrum in the dissipation range at frequencies higher than the proton gyroresonant frequency in the local magnetic field (see Figure 1). Interpretation of SOHO/UVCS observations of heavy ion emission suggests that the heavy ion temperature is anisotropic with $T_\perp \gg T_\parallel$. The temperature anisotropy and the more than mass proportional heavy ion heating was interpreted as evidence for ion cyclotron wave heating [e.g., *Kohl et al.*, 1997; *Li et al.*, 1998; *Cranmer et al.*, 1999a]. Preferential heavy ion heating was observed in situ by SWICS instrument on Ulysses [e.g., *von Steiger et al.*, 1995; *Reisenfeld et al.*, 2001], and recently by the Wind spacecraft [*Kasper et al.*, 2008].

[3] Coronal observations by TRACE and Hinode in EUV indicate that density inhomogeneity exists on fine scales in coronal loop plasma held by the coronal magnetic field [e.g., *Aschwanden et al.*, 1999; *Aschwanden*, 2004; *Ofman and Wang*, 2008], and it appears that the fine scales become smaller as the resolution of the instruments is increased [e.g., *Berger and Asgari-Targhi*, 2009]. This suggests that the plasma inhomogeneity across the magnetic field is self-similar and persists to ion inertia range of scales. SOHO/LASCO observation show that small-scale inhomogeneous coronal density structures, such as plumes, extend to at least 30 R_s [*DeForest et al.*, 2001]. Based on observations of loops, one can assume that plumes contain small-scale density inhomogeneity across the magnetic field significantly below the LASCO instrument resolution.

[4] The acceleration and heating of the multi-ion fast solar wind plasma in a coronal hole by spectrum of Alfvén waves was studied by *Ofman* [2004] using a 2.5-D multifluid model. In that study it was shown that is possible to produce fast solar wind in coronal holes, driven by low-frequency (MHD) Alfvén waves. However, the heavy ions require additional momentum and heat input to achieve speed and temperature that matches observations. The resonant heating of the solar wind plasma by spectrum of ion cyclotron waves and by heavy ions beams in homogeneous multi-ion plasma was studied by *Ofman and Viñas* [2007] using a 2-D hybrid model

[1]Department of Physics, Catholic University of America, Washington, D. C., USA.
[2]Also at NASA Goddard Space Flight Center, Greenbelt, Maryland, USA.
[3]Visiting Associate Professor at Tel Aviv University, Tel Aviv, Israel.

Copyright 2010 by the American Geophysical Union.
0148-0227/10/2009JA015094

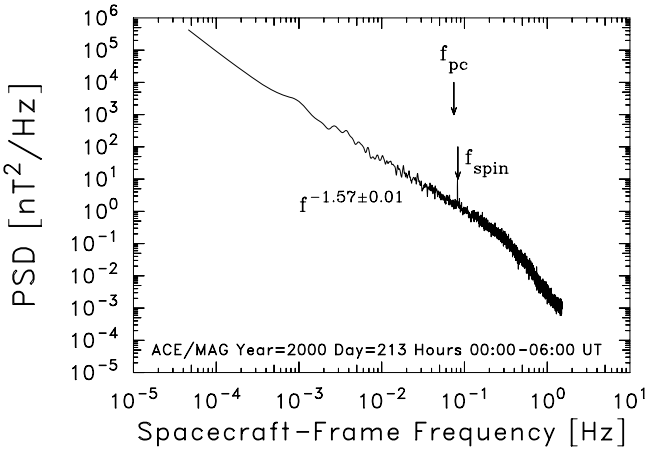

Figure 1. The typical form of the magnetic field fluctuation in the solar wind measured by ACE near 1 AU. A −1.57 power law fits well the spectrum in the inertial range. The break marking the onset of the dissipation range is visible in the spectrum. The proton cyclotron frequency f_{pc} and the spacecraft spin frequency f_{spin} in the spacecraft frame are indicated with arrows. Adapted from *Vasquez et al.* [2007].

for a small number of cases. In that study the spectrum of waves in the gyroresonant frequency range was launched in a localized region in the center of the 2-D domain. In the localized region, the magnetic field fluctuations were imposed externally, and were not consistent with other variables of the model.

[5] In the present model we extend the work of *Ofman and Viñas* [2007] by performing a parametric study, and by including a spectrum of waves launched at the boundary of the domain, allowing self-consistent solution in the computational 2-D domain. The effect of the source wave spectrum and beams on perpendicular heating of heavy ions is investigated for the first time in inhomogeneous plasma with density variation perpendicular to the background magnetic field. The resulting spectrum of waves in various regions of the computational domain was compared to observations. The use of a 2-D hybrid model allows the inclusion of parallel and oblique waves self consistently, and models the cross-field inhomogeneity. In the present study, we concentrate on a region close to the Sun (~10 R_s), in anticipation of future observations by the Solar Probe+ spacecraft [*McComas et al.*, 2008].

2. Hybrid Model

[6] In this section the 2-D hybrid simulation model is described [see also *Ofman and Viñas*, 2007]. In this model the ions are followed kinetically as particles in two-dimensional spatial domain, and the electrons are treated as neutralizing, massless background fluid. About six million particle velocity components per species are used to calculate the currents, the charge density, and the fields in the 2-D grid of 128 × 128 computational cell with an average of 127 particles per cell for each ion species (i.e., total of >4 × 10^6 particles). The size of the grid is in units of 1.5Δ, where $\Delta = c/\omega_{pp}$ is the proton inertia length, and $\omega_{pp} = (4\pi n_p e^2/m_p)^{1/2}$ is the proton plasma frequency. In physical units the inertia length is $\Delta = 2.3 \times 10^7/n_p^{1/2}$ cm. Using $n_p \approx 3 \times 10^3$ cm^{-3} at 10 R_s [see *Guhathakurta et al.*, 1999] we get $\Delta \approx 4.2 \times 10^5$ cm, and the corresponding area of the simulation region is approximately $(8.1 \times 10^7 \text{ cm})^2$ corresponding to about 1.1″ × 1.1″ at a distance of 1 AU.

[7] Note that each model particle is in fact a "superparticle" representing many physical particles with the same position in 2-D space and in phase space. The exact number of physical particles that correspond to each superparticle is determined by the density normalization. We have chosen 5% He^{++} and 90% proton number densities for the plasma to model the solar wind. Cartesian coordinate system is used with the y direction along the uniform background magnetic field $B_0\mathbf{e}_y$. The perpendicular x direction is across the plasma inhomogeneity, and the z direction is the ignorable coordinate. The particles spatial distribution is initialized with nonuniform density that varies as a function of x (see below). The velocity distribution of the particles is initialized as Maxwellian. The ion equations of motion are

$$\frac{d\mathbf{x}_k}{dt} = \mathbf{v}_k \tag{1}$$

$$m_k \frac{d\mathbf{v}_k}{dt} = Z_k e\left(\mathbf{E} + \frac{\mathbf{v}_k \times \mathbf{B}}{c}\right), \tag{2}$$

where k index is for each ion species, m_k is the ion mass, Z_k is the charge number, e is the electron mass, c is the speed of light. The electric field $\mathbf{E}$ is determined from the electron momentum equation, solved by neglecting electron inertia (since $m_e \ll m_k$).

$$n_e m_e \frac{d\mathbf{v}_e}{dt} \approx 0 = -en_e\left(\mathbf{E} + \frac{\mathbf{v}_e \times \mathbf{B}}{c}\right), \tag{3}$$

where n_e is the electron density determined from the charge neutrality condition $n_e = \sum_k Z_k n_k$. The above equations are supplemented by Maxwell's equations $\nabla \times \mathbf{E} = -\frac{1}{c}\partial\mathbf{B}/\partial t$, and $\nabla \times \mathbf{B} = \frac{4\pi}{c}\mathbf{J}$, where the local current J is calculated from the charged particle motions, and with the requirement that the total net current is zero (see *Winske and Omidi* [1993] for a detailed description of the hybrid model).

3. Initial State and Boundary Conditions

[8] The hybrid simulations were initiated with inhomogeneous background density of protons and He^{++} ions (see Figure 2). The high-density region occupies about a third of the plane, and the peak density in the center of the high-density region is three times higher than the density outside for both, protons, and He^{++} ions. The expression for the proton and ion normalized density is given by

$$n_k(x) = n_{0,k}\left[1 + n_{0m}e^{-\left(\frac{x-x_0}{w}\right)^6}\right], \tag{4}$$

where x_0 is the location of the central symmetry axis, n_{0m} is the amplitude of the inhomogeneity (in this study we have used values of n_{0m} in the range 0–4, where $n_{0m} = 0$ corresponds to homogeneous plasma), $w = 38.4\Delta$ determines the sharpness of the boundary of the high-density region, and k is the index for protons, and He^{++} ions. This form of density structure was used by *Tsiklauri et al.* [2005] to initialize ion and electron density in particle-in-cell (PIC) study of Alfvén

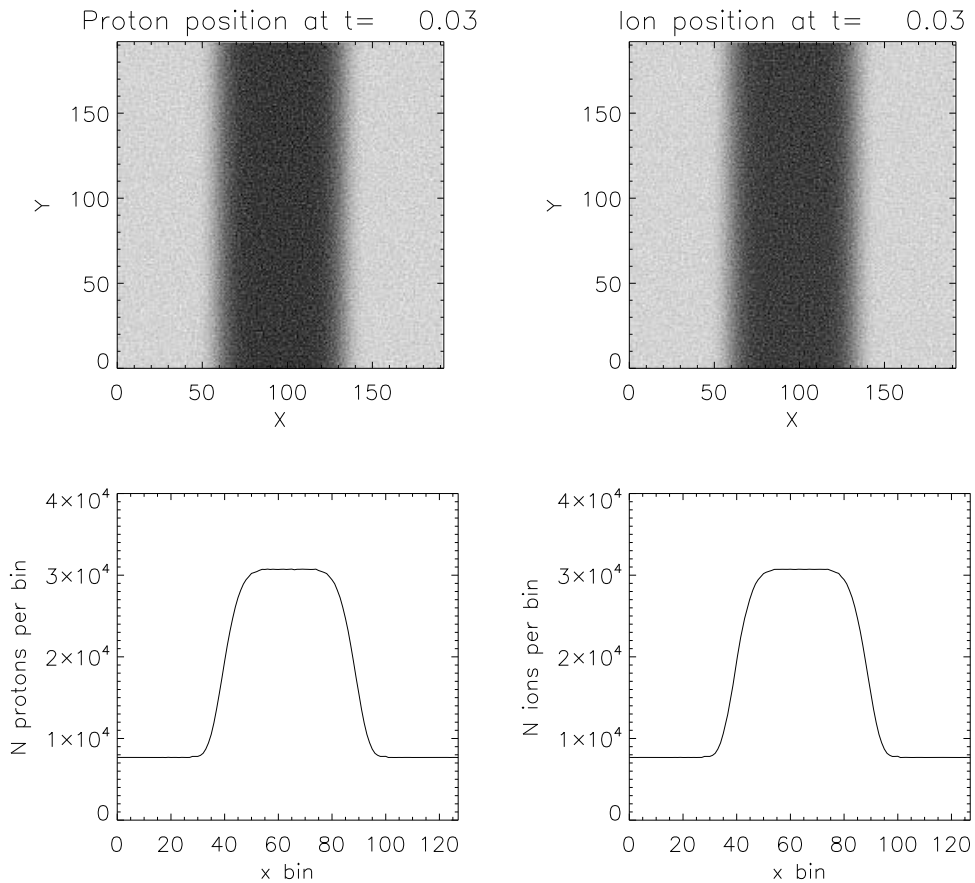

Figure 2. The initial density structure of (left) protons and (right) He^{++} ions. (top) The images show the 2-D density structure with the darkest level corresponding to about 250 particles per cell, and the brightest level corresponding to about 60 particles per cell for protons and He^{++} ions. (bottom) The number of particle dependence on x integrated in the y direction.

wave phase mixing. We use the above density profile to represent the cross-field inhomogeneity in plumes, and other magnetic structures in the solar wind.

[9] The normalization factors were $n_{0,p} = 0.9$, and $n_{0,He^{++}} = 0.05$. Thus, from charge neutrality $n_{0,e} = n_{0,p} + 2n_{0,He^{++}} = 1$. The electron fluid is assumed to be isothermal in this study. The initial temperature is isotropic and uniform for the electrons and ions. The ratio of the thermal and magnetic pressure is small everywhere. The electron plasma $\beta = 0.02$ in the uniform region. Therefore the inhomogeneous structure is held by the background magnetic pressure, as in solar coronal loops or plumes, and the total magnetic pressure is nearly uniform across the structure, i.e., for the electron fluid $B^2 + \beta_e n_{e,\max} \approx B^2 + \beta_e n_{e,\min} \approx B^2 = 1$ in normalized units, where $n_{e,\min}$ and $n_{e,\max}$, are the minimal and maximal electron density across the structure, respectively. This approximation holds for the total pressure as well since $\beta_i \sim \beta_e \ll 1$ in this study.

[10] Circularly polarized waves were driven by an f^{-1} power spectrum of waves at the simulation boundary at $x = 0$ and at $x = x_{\max}$ (see Figure 3). The temporal dependence of the magnetic fluctuations is given by

$$B_z(t) = B_{z0} b_0 \sum_{i=1}^{N} a_i \sin(\omega_i t + \Gamma_i), \tag{5}$$

where the mode amplitude $a_i = i^{-p/2}$, frequency $\omega_i = \omega_1 + (i-1)\Delta\omega$, the frequency range $\Delta\omega = (\omega_N - \omega_1)/(N-1)$, Γ_i is the random phase, and N is the number of modes, and b_0 is the normalization parameter. The value of p is 1, and $N = 100$. The value of B_{z_0} was varied and is given below. Since the boundary conditions were periodic in x and y directions the driving wave spectrum was forced to be periodic in x, by assigning the values of B_z at the last and penultimate grid points with the values of B_z at the second and the first grid points, respectively. The coupling to B_x was produced self-consistently through the Maxwell and Lorentz equations. The integration method for particle and field equations was the second-order rational Runge-Kutta method in time, and the spatial derivatives were calculated by pseudospectral FFT method. The waves were generated by imposing time dependent fluctuations in B_z with amplitude of 3% of the background field. The frequency band of the waves was below the proton gyroresonant frequency, but includes the He^{++} gyroresonant frequency in the plasma rest frame. The background magnetic field was uniform in the y direction. The circular polarization was obtained self consistently by the induced variation in (B_x, B_z), as evident in Figure 4. The waves propagated into the computational domain, and were refracted into the high-density region, due to the form of the background density and the corresponding Alfvén speed profile across the background magnetic field.

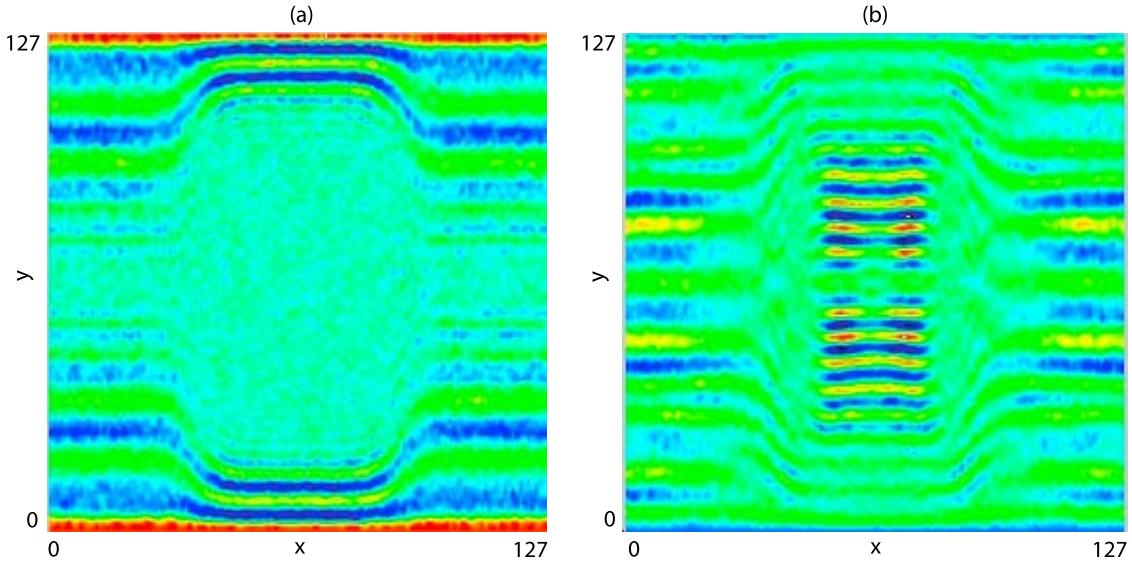

Figure 3. A snapshot of the driving Alfvén waves injected from the x boundaries as evident in B_z. (a) Near the beginning of the run. (b) Near the midtime of the run. Red indicates negative, blue indicates positive values of B_z, and green is zero. The maximal amplitude of B_z is 0.03. The coordinates are given in units of $\delta = 1.5c/\omega_{pp}$.

[11] For comparative study, a beam of He^{++} ions with drift (with respect to protons) velocities in the range $V_d = (1-2)V_A$ was initialized in the computational region, where $V_A = B/(4\pi\rho)^{1/2}$ is the Alfvén speed, and ρ is the mass density. Since, $V_d > V_A$ the configuration is ion cyclotron unstable leading to perpendicular beam heating [e.g., *Gary*, 1993; *Daughton and Gary*, 1998; *Daughton et al.*, 1999; *Xie et al.*, 2004; *Ofman and Viñas*, 2007]. The beam was used to excite ion cyclotron waves self-consistently, and self-consistent quasi-steady state was achieved in the nonlinear regime [*Ofman and Viñas*, 2007].

[12] The region of applicability of the model parameters is at about 10 solar radii from the Sun. The Alfvén speed in this region drops to ~300 km/s from ~1000 km/s in the lower corona due to the faster decreased of the magnetic field intensity, compared to the decrease of square root of density with heliocentric distance [e.g., *Collier et al.*, 2001; *Gopalswamy et al.*, 2001]. The value of β in this region is still $\ll 1$, in agreement with the parameter regime of the present study, since models show that the solar wind temperature has decreased by a factor of 2–3 at 10 R_s compared to the coronal values close to the Sun [e.g., *Cuperman et al.*, 1990; *Ofman*, 2004], and the corresponding sound speed is ~100 km/s.

[13] Although, at present the streaming parameters of He^{++} ions are unknown in this region, we can use observations of O VI ions by SOHO/UVCS as an indication of the possible values of differential streaming, as well as in situ observations by Helios, and Ulysses at 0.3 AU and beyond that show differential streaming of He^{++} ions by about an Alfvén speed [*Marsch et al.*, 1982a, 1982b; *Feldman et al.*, 1996; *Neugebauer et al.*, 2001]. For example, SOHO/UVCS observations indicated that O VI ions flow faster by about 300 km/s than protons at 3.5 R_s in a coronal hole [*Cranmer et al.*, 2008]. Using the coronal parameters obtained empirically by *Cranmer et al.* [1999b] we obtain $\beta_e \sim 0.02$ in that region, assuming 5 G at the coronal hole solar boundary [see *Ofman et al.*, 2001]. We find that the Alfvén speed is about 900 km/s in that region. If we assume that the differential streaming seen at 3.5 R_s is unchanged as the solar wind expands to 10 R_s, then the streaming will become super-Alfvénic at 10 R_s due to the faster drop of the magnetic field compared to the drop in density. The estimated plasma beta is decreased further by the drop in electron temperature over this distance. Although the above estimate is qualitative, at present we do not have the desired observations in this region

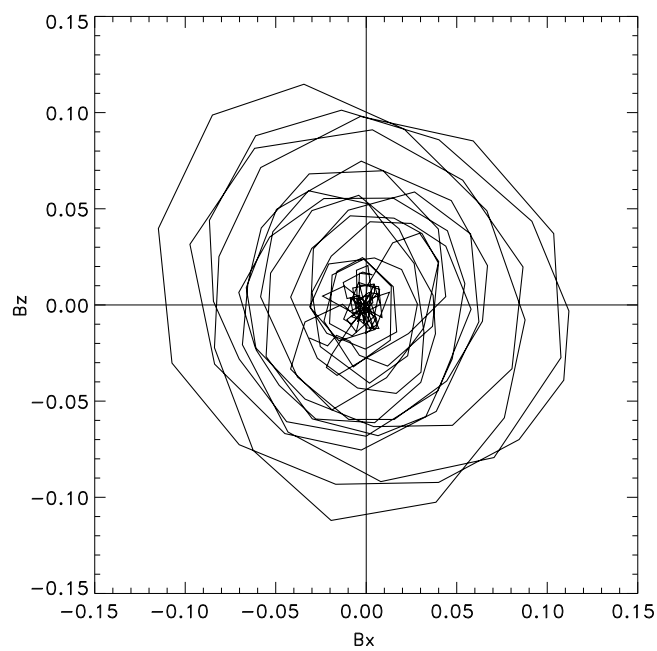

Figure 4. The perpendicular magnetic phase space plot showing the circularly polarized waves generated in the middle of the simulation region by the boundary driver. The growth of the perpendicular magnetic fluctuations with time is evident.

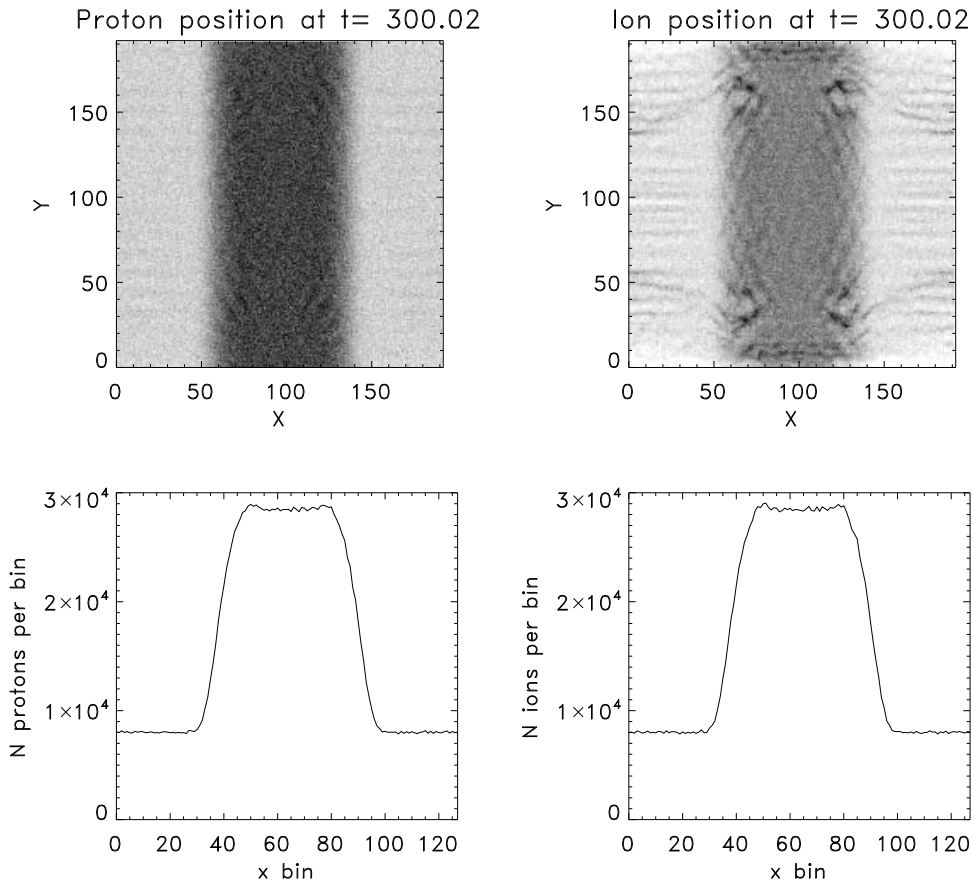

Figure 5. The density structure of (left) protons and (right) He^{++} ions at $t = 250\ \Omega_p^{-1}$ for the driven spectrum case. (top) The images show the 2-D density structure with the darkest level corresponding to about 280 particles and about 420 particles per cell for protons and He^{++} ions, respectively. The brightest level corresponds to about 35 particles per cell for protons and about 3 particles per cell for He^{++} ions. (bottom) The number of particle dependence on x integrated in the y direction.

to better estimate the parameters of the model. Therefore, we present a parametric study of the model.

4. Numerical Results

[14] In Figures 3–15 the results of the 2-D hybrid model of inhomogeneous solar wind plasma is shown. Figures 5 (left) and 5 (right) show the density structure of the protons and He^{++} ions, respectively, at $t = 300\ \Omega_p^{-1}$ for the driven spectrum case with $B_{z0} = 0.03$. Figure 5 (top) shows the density structure in two dimensions. The wave patterns in the density structure is due to the nonlinear compression by the Alfvén waves, and the refraction of the Alfvén wavefront by the inhomogeneous density profile. Note that the He^{++} ions are affected more significantly than protons, as evident in the density structure. The integrated density structure across the inhomogeneity was obtained by integrating the number of computational particles in the y direction. Figure 5 (bottom) shows that the density contrast and structure across the inhomogeneity did not change significantly throughout the evolution. The integrated small-scale fluctuations are somewhat stronger in the high-density region compared to the low-density region.

[15] In Figure 6 the temporal evolution of the temperature anisotropy of protons, He^{++} ions, and the $He^{++} - p$ drift for the run in Figure 5 are shown. It is evident that the He^{++} temperature anisotropy increases with time to $A_i = T_\perp/T_\parallel = W_\perp/2W_\parallel \approx 5.8$ at the peak. During the same period the proton temperature remained nearly isotropic. Inspecting the perpendicular ($W_{k,\perp} \propto \sum v_{k,\perp}^2$) and parallel ($W_{k,\parallel} \propto \sum v_{k,\parallel}^2$) kinetic energies shows that $W_{p,\perp}$, $W_{p,\parallel}$, and $W_{He++,\parallel}$ remain practically constant throughout the evolution, while $W_{He++,\perp}$ increases by a factor of 7.7 from the initial to final state. The drift velocity remains negligible throughout the run in this case (see Figure 6c).

[16] The spatial structure of the density for the run with $He^{++} - p$ drift of $V_d = 2\ V_A$ is shown in Figure 7 at $t = 50\ \Omega_p^{-1}$. The drift velocity is in the unstable regime with respect to ion cyclotron instability and leads to rapid heating [e.g., see *Ofman and Viñas*, 2007]. In the inhomogeneous density case we see evidence of the generation of small-scale density fluctuations associated with the magnetosonic waves in the high-density region. The waves are damped rapidly due to the gyroresonance with the He^{++} ion velocity distribution, and contribute to the dissipation of the free energy in the beam. As in the driven wave spectrum case, the effect is stronger for He^{++} ions than for protons. The small-scale structure produced by the beam instability is also evident in the integrated density profiles in the high-density region (Figure 7, bottom). Note that the local Alfvén speed varies across the structure,

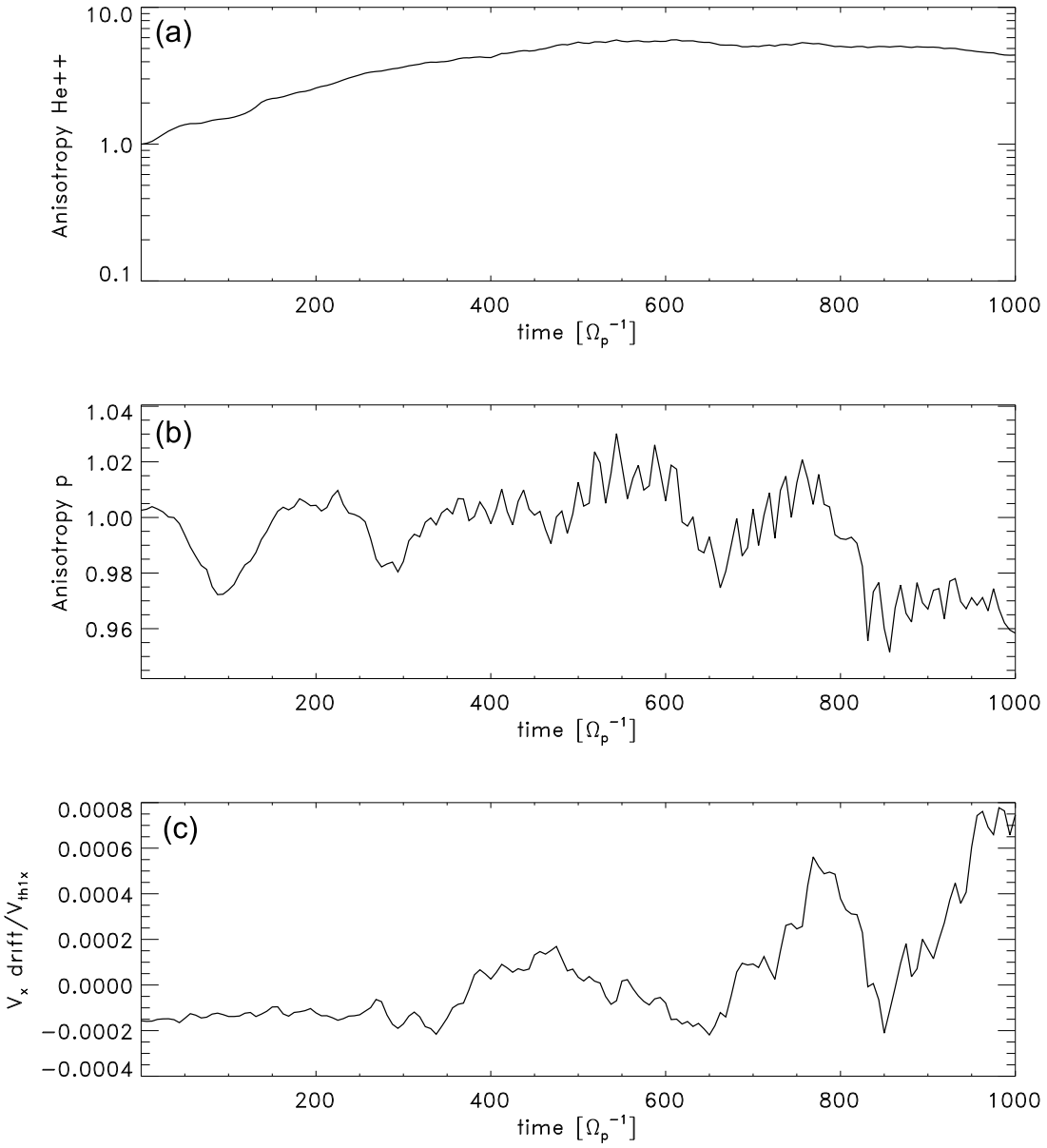

Figure 6. The temporal evolution of (a) He^{++} temperature anisotropy, (b) proton temperature anisotropy, and (c) the $He^{++} - p$ drift velocity with driven wave spectrum.

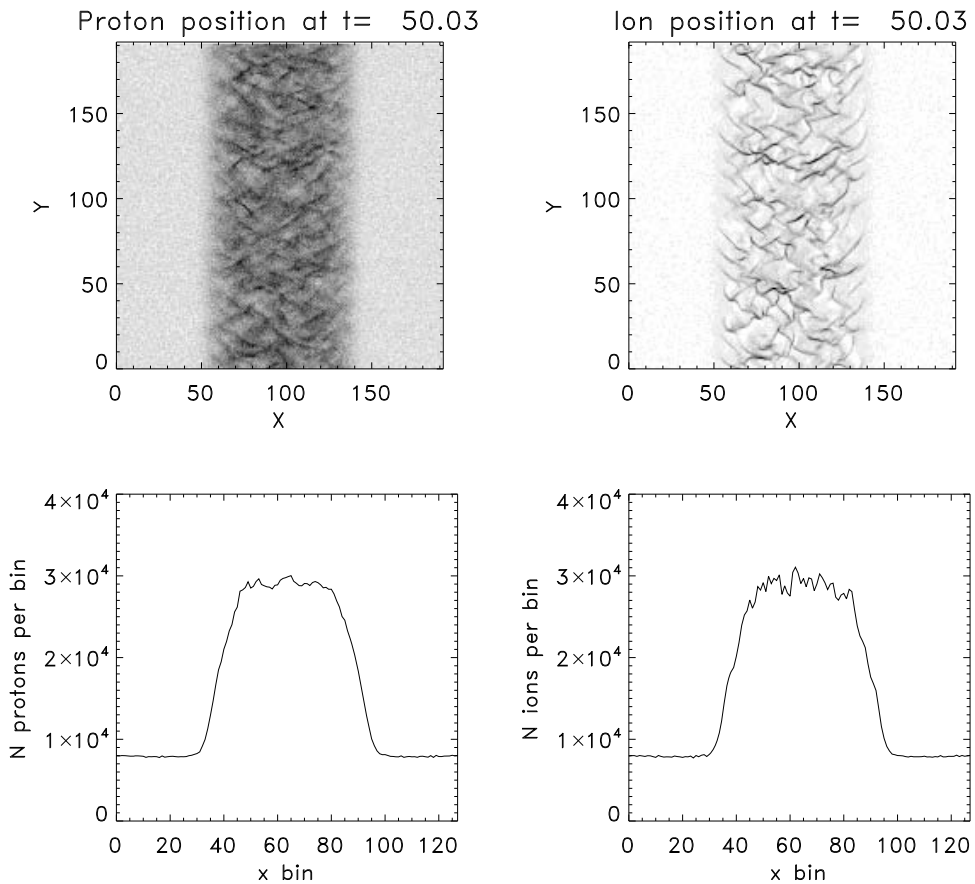

Figure 7. The density structure of (left) protons and (right) He^{++} ions at $t = 50\ \Omega_p^{-1}$ for $V_d = 2\ V_A$. (top) The images show the 2-D density structure with the darkest level corresponding to about 380 particles and about 1030 particles per cell for protons and He^{++} ions, respectively. The brightest level corresponds to about 36 particles per cell for protons and about 20 particles per cell for He^{++} ions. (bottom) The number of particle dependence on x integrated in the y direction.

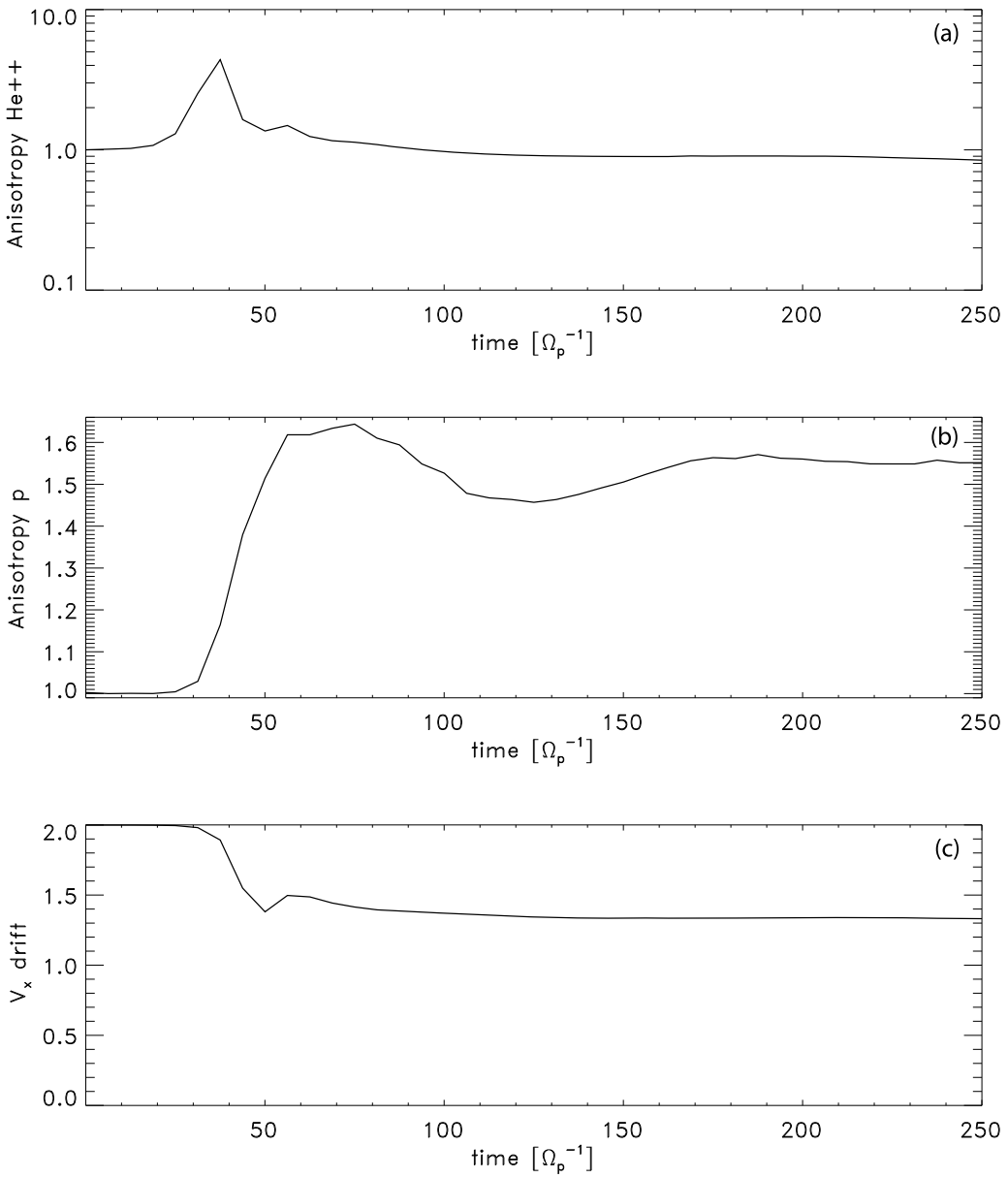

Figure 8. The temporal evolution of (a) He^{++} temperature anisotropy, (b) proton temperature anisotropy, and (c) the $He^{++} - p$ drift velocity with initial drift of $V_d = 2\ V_A$.

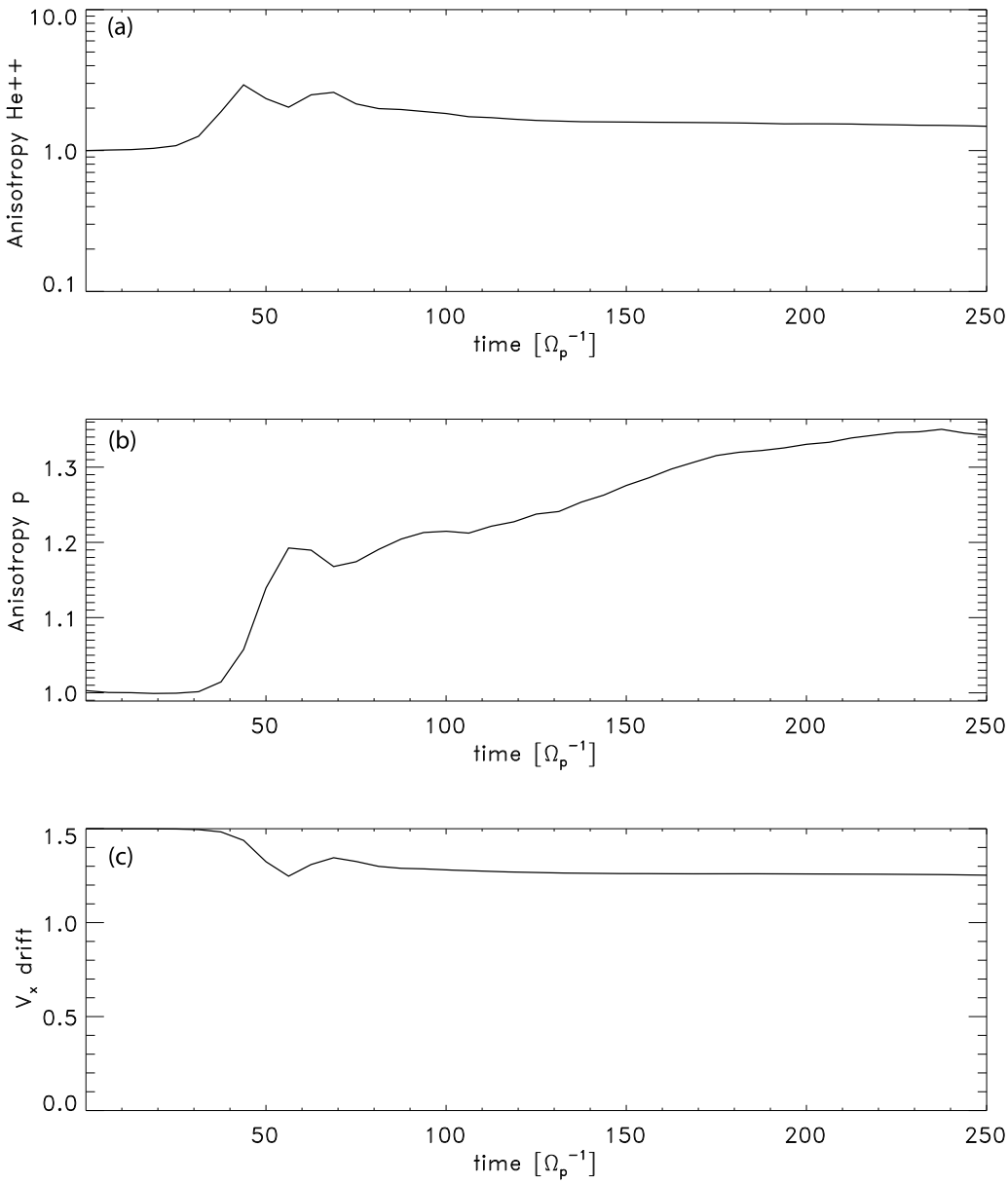

Figure 9. The temporal evolution of (a) He^{++} temperature anisotropy, (b) proton temperature anisotropy, and (c) $He^{++} - p$ drift velocity with initial drift of $V_d = 1.5\ V_A$.

and is smaller by a factor of $3^{1/2}$ in the high-density region. Thus, the beam is more super-Alfvénic there compared to the adjacent regions. At the end of the run ($t = 250\ \Omega_p^{-1}$) the small-scale structures are smoothed out, and are less apparent (not shown).

[17] The temporal evolution of the temperature anisotropy and the drift velocity are shown in Figure 8 for the run described in Figure 7. It is evident that the temperature anisotropy of He^{++} ions increases rapidly to about 4 within less than 40 Ω_p^{-1}. At the same time proton temperature anisotropy increased by 35% and the drift velocity begin do decrease. Following the peak of the He^{++} temperature anisotropy, we see rapid decline, with an asymptotic value slightly below 1 due to parallel heating. The protons continue to experience perpendicular heating, and their anisotropy increases to nearly 1.7. During this evolution, the relative drift decreases to 1.5 V_A, and continues more gradual decrease to about 1.3 V_A at the end of the run ($t = 250\ \Omega_p^{-1}$). Inspecting the parallel and perpendicular energy evolution shows that for protons $W_{p,\perp}(t = 250\ \Omega_p^{-1})/W_{p,\perp}(t = 0) = 2.2$, while for He^{++} the ratio increases dramatically by a factor of 22.8. During the same period we find for protons $W_{p,\|}(t = 250)/W_{p,\|}(t = 0) = 1.4$, and $W_{He++,\|}(t = 250\ \Omega_p^{-1})/W_{He++,\|}(t = 0) = 30.4$. Thus, in this case we find that the super-Alfvénic beam leads to initial heating of He^{++} ions, followed by proton heating, and the heating is significant in both, parallel and perpendicular directions.

[18] The magnitude of the heating depends on the magnitude of the initial drift (see also the results of the parametric study below). To provide detailed evidence of this dependence, we show the results of the temporal evolution of the run with $V_d = 1.5\ V_A$ in Figure 9. In this case the evolution is

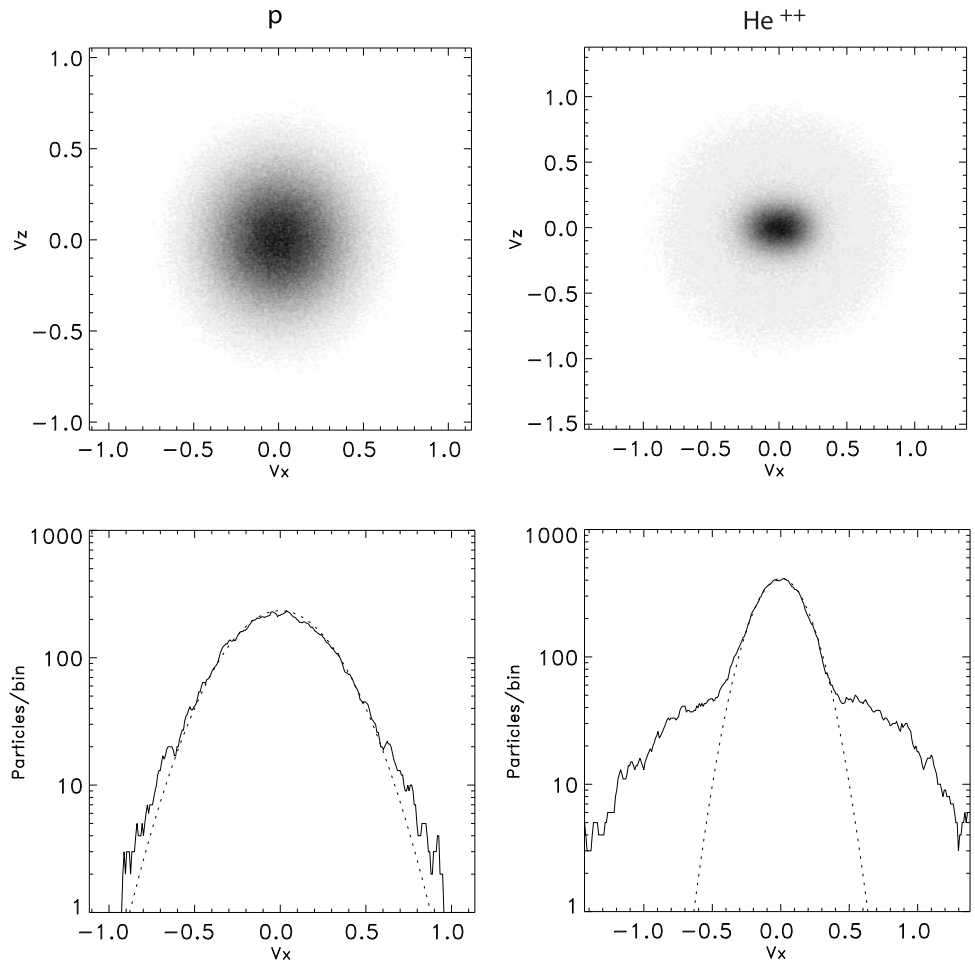

Figure 10. (top) The perpendicular velocity distributions at $t = 250\ \Omega_p^{-1}$ for protons and He^{++} ions for the case with $V_d = 2\ V_A$. (bottom) The cut through the peak of the velocity distribution showing the number of pericles per bin in velocity space. The dashed curves show the best fit Maxwellian distributions.

qualitatively similar to the evolution shown in Figure 8. However, the peak He^{++} temperature anisotropy is about 2, and the peak proton temperature anisotropy is 1.35, reached toward the end of the run. Inspecting parallel and perpendicular energy evolution for this case shows that $W_{p,\perp}(t = 250\ \Omega_p^{-1})/W_{p,\perp}(t = 0) = 1.3$, while for He^{++} the ratio increases by a factor of 8.5. During the same period we find $W_{p,\|}$ did not change significantly, and for He^{++} ions $W_{He++,\|}(t = 250\ \Omega_p^{-1})/W_{He++,\|}(t = 0) = 5.7$. Thus, in this case as well we see that the super-Alfvénic beam leads to initial heating of He^{++} ions, followed by proton heating, and the heating is significant in both, parallel and perpendicular directions for He^{++}. As expected, the lower drift speed ($V_d = 1.5\ V_A$) than in the previous case ($V_d = 2\ V_A$) results in smaller heating, and smaller anisotropy in the final stage. It is interesting to note that $V_d = 1.5\ V_A$ is marginally stable in homogeneous plasma ($n_{0m} = 0$).

[19] The perpendicular velocity distribution for protons and He^{++} ions for the case with $V_d = 2\ V_A$ is shown in Figure 10 at $t = 250\ \Omega_p^{-1}$. Figure 10 (left) shows protons, and Figure 10 (right) shows He^{++} ions. It is evident that the perpendicular distribution is centrally peaked, and can be approximated well with a Maxwellian for protons. The He^{++} ion perpendicular velocity distribution is Maxwellian in the center with and extended halo. This non-Maxwellian feature is the result of wave particle interaction and velocity space diffusion due to the waves generated by the drift instability.

[20] In the driven spectrum case with $B_{z_0} = 0.03$ shown in Figure 11 at $t = 543\ \Omega_p^{-1}$ the halo in the perpendicular velocity distribution of He^{++} ions is less significant than in the drifting case shown in Figure 10, and the velocity distribution is nearly Maxwellian for protons. The He^{++} velocity distribution can be approximated well by bi-Maxwellian distribution. Based on the present results, in situ observation of the He^{++} ion velocity distribution halos can be used to distinguish between the various heating scenarios.

[21] The dependence of the temperature anisotropy and $W_\perp$ of protons and He^{++} ions on the amplitude of the Alfvén wave spectrum B_{z_0} in the inhomogeneous plasma ($n_{0m} = 3$) is shown in Figure 12. It is evident that the maximal $W_\perp$ and maximal $A_{i,k}$ increases with B_{z_0} in most cases. For larger amplitude spectrum A_i decreases due to increased parallel heating of the He^{++} ions, while the perpendicular heating increases with B_{z_0} for all values. The increase of He^{++} perpendicular heating is more dramatic due to frequency range of the spectrum.

[22] Parametric studies of the initial drift in the inhomogeneous plasma on the results are shown in Figure 13. In Figure 13a the final drift velocity and the perpendicular

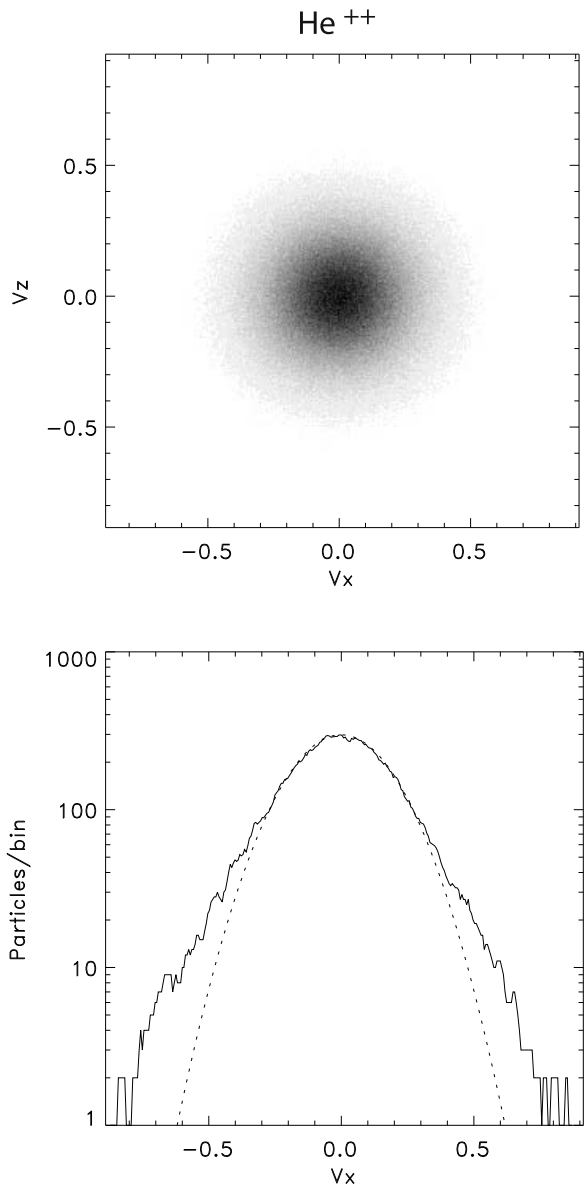

Figure 11. (top) The perpendicular velocity distributions at $t = 543\ \Omega_p^{-1}$ for He^{++} ions for the driven wave spectrum with $B_{z_0} = 0.03$. (bottom) The cut through the peak of the velocity distribution showing the number of pericles per bin in velocity space. The dashed curves show the best fit Maxwellian distribution.

kinetic energy ($W_\perp$) are shown as a function of the initial drift speed. When the initial drift exceeds ~1.2 V_A the plasma becomes unstable, in agreement with linear Vlasov's theory that predicts the onset of instability for super-Alfvénic drift that is also seen in 1-D hybrid [*Xie et al.*, 2004] and 2-D hybrid homogeneous plasma models [*Ofman and Viñas*, 2007]. Due to the instability that leads to velocity-space diffusion the final drift at the end of the runs decreases, while $W_{i,p,\perp}$ increases. The maximal proton and He^{++} temperature anisotropy is increasing for super-Alfvénic drift with the drift speed (Figures 13b). The time of the maximal anisotropy for protons is at $t > 200\ \Omega_p^{-1}$ for drifts below 2 V_A. However, for He^{++}, and for protons at $V_d = 2\ V_A$ the anisotropy peaks at about $t = 40\ \Omega_p^{-1}$, due to the faster evolution of the instability at higher drift speed. The temperature anisotropy at the end of the run for He^{++} has decreased from the maximal value due to relaxation by secondary ion cyclotron instability of the anisotropic He^{++} ion population.

[23] In Figure 14 the effect of the magnitude of inhomogeneity (n_{0m}) on the anisotropy is investigated for the drifting plasma with $V_d = 1.5\ V_A$. In Figure 14a the dependence of the anisotropy and the time to reach the maximal values on n_{0m} is shown. It is evident that for $n_{0m} \geq 2$ the maximal anisotropy increases with the inhomogeneity, and the time to reach the maximal A_i is generally decreasing. When $n_{0m} = 1$, the maximal A_i occurs after much longer time than for $n_{0m} \geq 2$. In the homogeneous case ($n_{0m} = 0$) the plasma is marginally stable and there is no significant perpendicular heating for $V_d = 1.5\ V_A$.

[24] In Figure 14b the dependence of the temperature anisotropy on n_{0m} is shown for the driven wave spectrum with $B_{z_0} = 0.03$. The proton temperature remains isotropic for all values of n_{0m}, while the He^{++} temperature anisotropy reaches the maximal value generally faster when n_{0m} is increased. The decrease in maximal anisotropy with n_{0m} is the result of parallel heating that becomes more significant at later times.

[25] In the context of solar wind observations discussed in the Introduction, and shown in Figure 1, we calculated the spectrum of magnetic fluctuations in the center of the domain for the driven spectrum and the $V_d = 2\ V_A$ beam cases. Figure 15 shows the spectrum for both cases in low-density and high-density regions. The best fit power law is shown with the dashed-dotted line. The power law was fit in the regions where the slope of the spectrum did not change considerably. It was found that in both cases the power law spectrum in the low-density region was significantly less steep than in the high-density region. The slope was $m = -1.66$ in the low-density region of the wave driven case, and $m = -1.81$ for the beam case. These values of the slope are close to −5/3, the slope associated with Kolmogorov turbulence in the inertial range of the spectrum (see Figure 1). The appearance of turbulent fluctuations is expected in the observations and the hybrid model, since the motions of protons and ions are random down to the kinetic scale. The particular slope of the power spectrum indicates whether the motions are in the inertial or the dissipation dominant regime. In the high-density region the slopes were $m = -2.53$ for the driven wave spectrum case, and $m = -2.80$ for the beam case, associated with the dissipation range Figure 1. The model shows that the dissipation was more significant in the high-density regions due to the refraction of Alfvén waves, and the generation of local magnetosonic fluctuations.

5. Discussion and Conclusions

[26] Using the 2-D hybrid model of inhomogeneous plasma we investigate the resonant heating of multicomponent solar wind plasma by a source spectrum of waves that resonate with ion gyromotions, and by unstable heavy ions beams that produce a spectrum of resonant waves that consequently leads to perpendicular heating of He^{++} and protons. The 2-D hybrid model allows the consideration of parallel and oblique waves in inhomogeneous plasma. Satellite coronal observations in EUV and white light indicate the appearance of cross-field inhomogeneities (loops and plumes) and small scales to

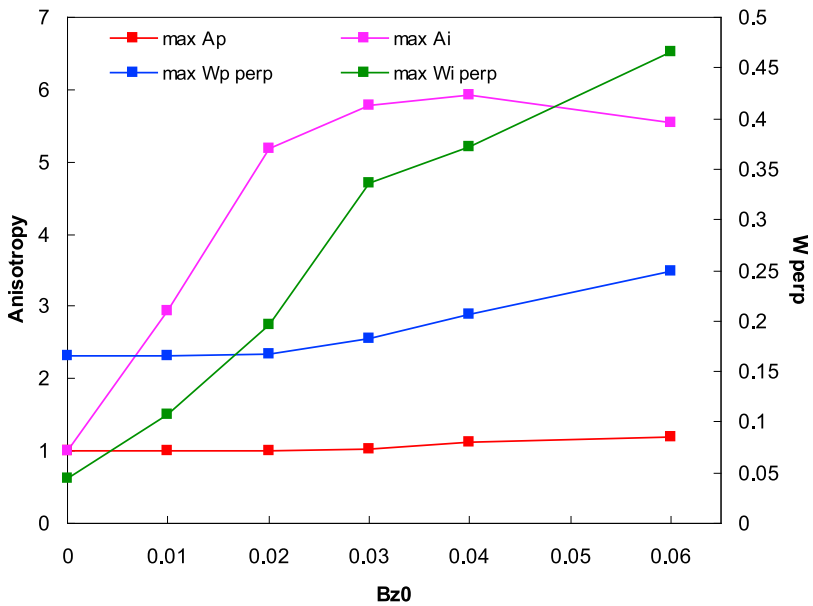

Figure 12. Parametric studies of the effect of the driven spectrum amplitude B_{z_0} on the maximal proton and He^{++} ion anisotropy and on the maximal perpendicular kinetic energy.

the resolution limit. Small-scale quasi-steady structures have been observed to extend to 30 R_s in coronal holes, regions of fast solar wind outflow. The spectrum of Alfvénic fluctuations, as well as drifting heavy ions by about an Alfvén speed have been measured in situ by Helios, and Ulysses spacecraft beyond 0.3 AU. We use the present model to perform a parametric study of the heating of the solar wind plasma in the small-scale inhomogeneous regions by Alfvén waves and drifting He^{++} ions.

[27] We find that the He^{++} ions are heated efficiently due to resonant interaction with driven left-hand polarized cyclotron wave spectrum below the proton gyroresonant frequency, while proton heating is not significant in this case. The heating of He^{++} ions occurs primarily in the perpendicular direction. The spectrum includes the He^{++} resonant frequency in the plasma rest frame. The density fluctuations generated in the inhomogeneous background density structure provide additional source of small-scale variability, and enhances the heating. The driving Alfvén waves are refracted by the background density inhomogeneity, due to the variation of the local Alfvén speed. Evidently, the study of the refraction requires (at least) a 2-D model.

[28] We find that the velocity distribution of the ions heated by broadband spectrum of cyclotron waves can be approximated well by bi-Maxwellian distribution at the end of the evolution. The low-amplitude high-frequency waves (i.e., $\omega \sim \Omega_i$) that are present in the solar wind, and likely in corona lead to heavy ion perpendicular heating. Since the heavy ion resonant frequency, and in particular He^{++} resonance is below the proton resonant frequency, the heating of protons is limited to the part of the wave energy spectrum, not absorbed, or re-emitted by heavy ions due to instability in the heavy ion population. This scenario is confirmed by the hybrid simulation study that shows lesser heating of protons than heavy

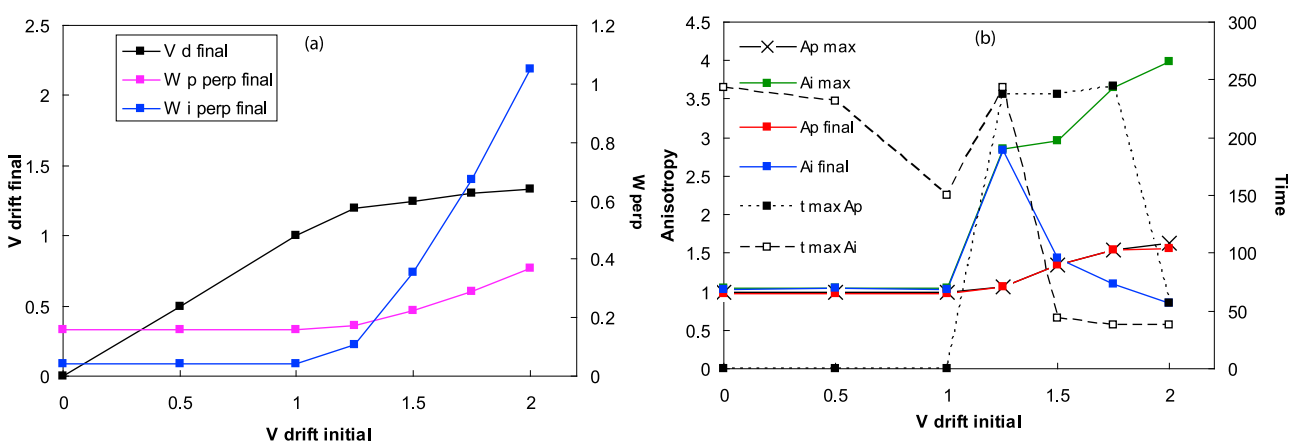

Figure 13. Parametric studies of the effect of the initial drift on (a) the final drift and the perpendicular kinetic energy and (b) proton and He^{++} ion anisotropy (maximal and final) and on the time of the maximal temperature anisotropy.

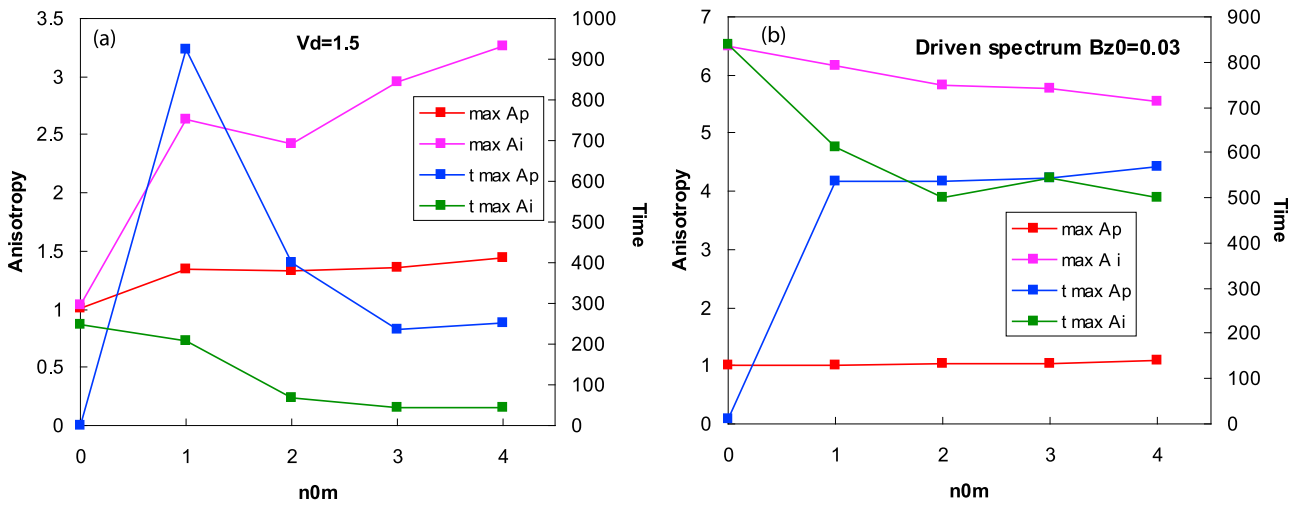

Figure 14. Parametric studies of the effect of the inhomogeneity amplitude n_{0m} on the temperature anisotropy with (a) $V_d = 1.5\ V_A$ and (b) driven spectrum with $B_{z_0} = 0.03$.

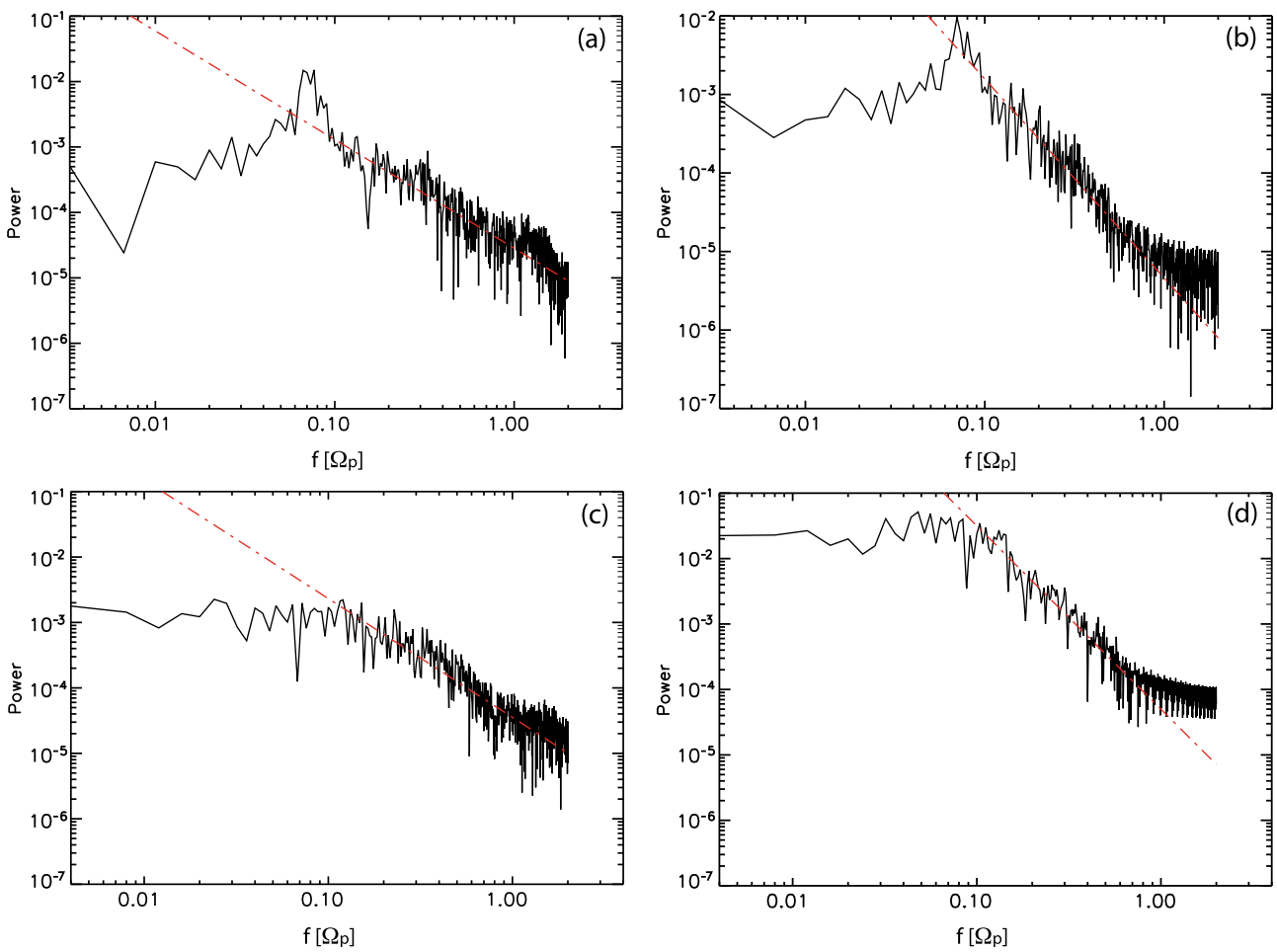

Figure 15. The power spectrum of fluctuations in B_z. (a) Middle of low-density region, driven waves spectrum. The dashed line is for power law fit with $m = -1.66$. (b) Same as Figure 15a, but in the middle of high-density region. The fit is with $m = -2.53$. (c) Middle of the low-density region, the case with $V_d = 2\ V_A$. The dashed line is for power law fit with $m = -1.81$. (d) Same as Figure 15c, but in the middle of the high-density region. The dashed line is for power law fit with $m = -2.80$.

ions. We find that as a result of inhomogeneity the He^{++} heating is more significant than in homogeneous plasma, while small proton heating is increasing with inhomogeneity as well.

[29] We also investigate the heating of protons and He^{++} ions due the instability of the super-Alfvénic drift, and find that both, protons and He^{++} ions are heated significantly in perpendicular and parallel directions for $V_d \geq 1.5\ V_A$. We find that He^{++} are heated first anisotropically ($T_\perp > T_\parallel$), followed by parallel heating, and proton heating that proceeds in a similar way. We also find that the heating of He^{++} is larger by an order of magnitude than for protons for $V_d \geq 1.5\ V_A$. We find that the heating is significantly stronger and faster when inhomogeneity is present as evident from the parametric study.

[30] We investigate the dependence of the temperature anisotropy and the perpendicular heating on the parameters of the model. Parametric studies of the driven wave spectrum show that for small amplitude the temperature anisotropy and the perpendicular heating increases monotonically with B_{z0}, with small decrease of A_p for larger amplitudes, due to the effect of increased parallel heating. The parallel heating becomes more significant when B_{z0} is increased due to the increased effect of the parallel wave pressure gradient, proportional to $\nabla(\delta B^2)$, where δB is the amplitude of the wave magnetic fluctuations. We find that the maximal temperature anisotropy and the perpendicular heating increases with the drift speed. The relaxation of the drift instability results in the decrease of the final drift speed, while the final ion anisotropy decreases due to secondary ion cyclotron instability of the He^{++} population.

[31] Parametric study of the effect of the inhomogeneity shows that for the drifting case the maximal temperature anisotropy of protons and He^{++} ions generally increases with n_{0m}, while the time to reach the maximal value generally decreases. When the inhomogeneity parameter is increased for the driven Alfvén wave spectrum that heats the He^{++} ions, the result is lower He^{++} maximal anisotropy due to increased parallel heating of the ions. The time to reach the maximal anisotropy generally decreases for He^{++}. The effect of the driving spectrum on proton heating is small for all values of inhomogeneity considered in this study.

[32] We compare the spectra of magnetic fluctuations generated in our model to the observed power spectrum of magnetic fluctuations in the solar wind. We find that both, inertial range spectrum and dissipation range spectrum are generated in our hybrid model, similar to solar wind observations (see Figure 1). The inertial range is produced in low-density regions, where the dissipation effects are small. In regions where the dissipation is enhanced due to the generation of magnetosonic fluctuations, we see steeper spectrum of fluctuations, consistent with observations. The results of this study could possibly be tested in the future by Solar Probe+ [*McComas et al.*, 2008] that will cross solar wind streams in the inner solar wind, and measure magnetic fluctuations in the inhomogeneous solar wind plasma below 10 R_s.

[33] **Acknowledgments.** The author would like to acknowledge discussions with A. F. Viñas and D. Tsiklauri and to acknowledge support by NASA grants NNX08AF85G and NNX08AV88G.

[34] Philippa Browning thanks the reviewers for their assistance in evaluating this paper.

References

Aschwanden, M. J. (2004), *Physics of the Solar Corona: An Introduction*, Praxis, Chichester, U. K.

Aschwanden, M. J., L. Fletcher, C. J. Schrijver, and D. Alexander (1999), Coronal loop oscillations observed with the Transition Region and Coronal Explorer, *Astrophys. J.*, *520*, 880–894.

Berger, M. A., and M. Asgari-Targhi (2009), Self-organized braiding and the structure of coronal loops, *Astrophys. J.*, *705*, 347–355, doi:10.1088/0004-637X/705/1/347.

Collier, M. R., et al. (2001), Reconnection remnants in the magnetic cloud of October 18–19, 1995: A shock, monochromatic wave, heat flux dropout, and energetic ion beam, *J. Geophys. Res.*, *106*, 15,985–16,000, doi:10.1029/2000JA000101.

Cranmer, S. R., G. B. Field, and J. L. Kohl (1999a), Spectroscopic constraints on models of ion cyclotron resonance heating in the polar solar corona and high-speed solar wind, *Astrophys. J.*, *518*, 937–947.

Cranmer, S. R., et al. (1999b), An empirical model of a polar coronal hole at solar minimum, *Astrophys. J.*, *511*, 481–501, doi:10.1086/306675.

Cranmer, S. R., A. V. Panasyuk, and J. L. Kohl (2008), Improved constraints on the preferential heating and acceleration of oxygen ions in the extended solar corona, *Astrophys. J.*, *678*, 1480–1497, doi:10.1086/586890.

Cuperman, S., L. Ofman, and M. Dryer (1990), Thermally conductive magnetohydrodynamic flows in helmet-streamer coronal structures, *Astrophys. J.*, *350*, 846–855, doi:10.1086/168436.

Daughton, W., and S. P. Gary (1998), Electromagnetic proton/proton instabilities in the solar wind, *J. Geophys. Res.*, *103*, 20,613–20,620, doi:10.1029/98JA01385.

Daughton, W., S. P. Gary, and D. Winske (1999), Electromagnetic proton/proton instabilities in the solar wind: Simulations, *J. Geophys. Res.*, *104*, 4657–4668, doi:10.1029/1998JA900105.

DeForest, C. E., S. P. Plunkett, and M. D. Andrews (2001), Observation of polar plumes at high solar altitudes, *Astrophys. J.*, *546*, 569–575, doi:10.1086/318221.

Feldman, W. C., B. L. Barraclough, J. L. Phillips, and Y.-M. Wang (1996), Constraints on high-speed solar wind structure near its coronal base: A ULYSSES perspective, *Astron. Astrophys.*, *316*, 355–367.

Gary, S. P. (1993), *Theory of Space Plasma Microinstabilities*, Cambridge Univ. Press, New York.

Gopalswamy, N., A. Lara, M. L. Kaiser, and J. Bougeret (2001), Near-Sun and near-Earth manifestations of solar eruptions, *J. Geophys. Res.*, *106*, 25,261–25,278, doi:10.1029/2000JA004025.

Guhathakurta, M., A. Fludra, S. E. Gibson, D. Biesecker, and R. Fisher (1999), Physical properties of a coronal hole from a coronal diagnostic spectrometer, Mauna Loa Coronagraph, and LASCO observations during the Whole Sun Month, *J. Geophys. Res.*, *104*, 9801–9808, doi:10.1029/1998JA900082.

Kasper, J. C., A. J. Lazarus, and S. P. Gary (2008), Hot solar-wind helium: Direct evidence for local heating by Alfvén-cyclotron dissipation, *Phys. Rev. Lett.*, *101*(26), 261103, doi:10.1103/PhysRevLett.101.261103.

Kohl, J. L., et al. (1997), First results from the SOHO Ultraviolet Coronagraph Spectrometer, *Sol. Phys.*, *175*, 613–644.

Li, X., S. R. Habbal, J. Kohl, and G. Noci (1998), The effect of temperature anisotropy on observations of Doppler dimming and pumping in the inner corona, *Astrophys. J.*, *501*, L133–L137.

Marsch, E., K.-H. Mühlhäuser, H. Rosenbauer, R. Schwenn, and F. M. Neubauer (1982a), Solar wind helium ions: Observations of the Helios solar probes between 0.3 and 1 AU, *J. Geophys. Res.*, *87*(A1), 35–51.

Marsch, E., K.-H. Mühlhäuser, R. Schwenn, H. Rosenbauer, W. Pilipp, and F. M. Neubauer (1982b), Solar wind protons: Three-dimensional velocity distributions and derived plasma parameters measured between 0.3 and 1 AU, *J. Geophys. Res.*, *87*(A1), 52–72.

McComas, D. J., et al. (2008), Solar Probe Plus: Report of the Science and Technology Definition Team, *NASA Tech. Memo., NASA/TM-2008-214161*.

Neugebauer, M., B. E. Goldstein, D. Winterhalter, E. J. Smith, R. J. MacDowall, and S. P. Gary (2001), Ion distributions in large magnetic holes in the fast solar wind, *J. Geophys. Res.*, *106* 5635–5648, doi:10.1029/2000JA000331.

Ofman, L. (2004), Three-fluid model of the heating and acceleration of the fast solar wind, *J. Geophys. Res.*, *109*, A07102, doi:10.1029/2003JA010221.

Ofman, L., and A. F. Viñas (2007), Two-dimensional hybrid model of wave and beam heating of multi-ion solar wind plasma, *J. Geophys. Res.*, *112*, A06104, doi:10.1029/2006JA012187.

Ofman, L., and T. J. Wang (2008), Hinode observations of transverse waves with flows in coronal loops, *Astron. Astrophys.*, *482*, L9–L12, doi:10.1051/0004-6361:20079340.

Ofman, L., A. Viñas, and S. P. Gary (2001), Constraints on the O^{+5} anisotropy in the solar corona, *Astrophys. J.*, *547*, L175–L178, doi:10.1086/318900.

Reisenfeld, D. B., S. P. Gary, J. T. Gosling, J. T. Steinberg, D. J. McComas, B. E. Goldstein, and M. Neugebauer (2001), Helium energetics in the high-latitude solar wind: Ulysses observations, *J. Geophys. Res.*, *106*, 5693–5708, doi:10.1029/2000JA000317.

Tsiklauri, D., J.-I. Sakai, and S. Saito (2005), Particle-in-cell simulations of circularly polarised Alfvén wave phase mixing: A new mechanism for electron acceleration in collisionless plasmas, *Astron. Astrophys.*, *435*, 1105–1113, doi:10.1051/0004-6361:20042436.

Vasquez, B. J., C. W. Smith, K. Hamilton, B. T. MacBride, and R. J. Leamon (2007), Evaluation of the turbulent energy cascade rates from the upper inertial range in the solar wind at 1 AU, *J. Geophys. Res.*, *112*, A07101, doi:10.1029/2007JA012305.

von Steiger, R., J. Geiss, G. Gloeckler, and A. B. Galvin (1995), Kinetic properties of heavy ions in the solar wind from SWICS/Ulysses, *Space Sci. Rev.*, *72*, 71–76, doi:10.1007/BF00768756.

Winske, D., and N. Omidi (1993), *Computer Space Plasma Physics: Simulation Techniques and Sowftware*, edited by H. Matsumoto and Y. Omura, pp. 103–160, Terra Sci., Tokyo.

Xie, H., L. Ofman, and A. Viñas (2004), Multiple ions resonant heating and acceleration by Alfvn/cyclotron fluctuations in the corona and the solar wind, *J. Geophys. Res.*, *109*, A08103, doi:10.1029/2004JA010501.

L. Ofman, NASA Goddard Space Flight Center, Code 671, Greenbelt, MD 20771, USA. (leon.ofman@nasa.gov)